Full Paper

Investigations of Cu/Zn Oxalates from Aqueous Solution: Single-Phase Precursors and Beyond

Leon Zwiener,[a] Dr. Frank Girgsdies,[a] Prof.^^Dr. Robert Schlögl,[a,b] and Dr. Elias Frei[a]

[a] Department of Inorganic Chemistry
Fritz-Haber-Institut der Max-Planck-Gesellschaft
Faradayweg 4 - 6, 14195 Berlin (Germany)
E-mail: efrei@fhi-berlin.mpg.de

[b] Department of Heterogeneous Reactions
Max-Planck-Institut für Chemische Energiekonversion
Stiftstrasse 34 - 36, 45470 Mülheim an der Ruhr (Germany)

Abstract

The existence of a limited solid-solution series in the Cu/Zn binary metal oxalate system is reported. Coprecipitation was applied for the preparation of a comprehensive set of mixed Cu/Zn oxalates. Rietveld refinement of the XRD data revealed the formation of mixed-metal oxalate single phases at the compositional peripheries. Accordingly, the isomorphous substitution of Zn^{II} into Cu^{II} oxalate takes place at Zn contents of ≤6.6 and ≥79.1 atom%. Zn incorporation leads to a pronounced unit-cell contraction accompanied by Vegard-type trends for the lattice parameters. Morphologically, both solid solutions show close resemblance to the corresponding pure single-metal oxalates, and thus distinct differences are identified (SEM). The successful formation of solid solutions was further evidenced by thermal analysis. The decomposition temperature of the oxalate was taken as an approximation for Zn^{II} incorporation into the Cu^{II} oxalate structure. Single decomposition events are observed within the stated compositional boundaries and shift to higher temperature with increasing Zn content, whereas multiple events are present

near Cu/Zn parity. Moreover, these findings are supported by IR and Raman spectroscopic investigations. This study on the Cu/Zn mixed-metal oxalate system sheds light on the important prerequisites for solid-solution formation and identifies the structural limitations that predefine its application as catalyst precursor.

Introduction

Oxalic acid, the simplest dicarboxylic acid, is widely distributed in nature, including fungi, lichens, plants, and animals.[1] Its ready formation of metal oxalates leads to a broad diversity of different salts and complexes of alkali metals, alkaline earth metals, transition metals including copper and zinc, and rare earth elements.[2] Most simple oxalates are insoluble in water.[2] Hence, naturally occurring oxalates constitute the largest group of carboxylate minerals and the most common group of organic minerals,[3] including moolooite, a naturally occurring hydrated copper oxalate, first reported in the mid-1980s by Clarke and Williams.[4] In addition, synthetic metal oxalates such as those of copper and zinc are widely investigated as precursors in the synthesis of nanomaterials[5] and catalysts.[6] The fast and easy process of precipitation of metal oxalates from aqueous solutions and the subsequent emission of volatile CO and CO_2 during their thermal decomposition to metals or metal oxides[7] makes them ideal precursor phases. A joint cationic sublattice allows a high degree of Cu/Zn substitution and therefore nanoscale intermixing as a central prerequisite for highly dispersed Cu/ZnO particles in the final catalyst.[8] Copper(II) oxalate $CuC_2O_4{\cdot}n$^H_2O ($0 \le n \le 1$[3,4,9]) holds a special position in the group of first-row transition metal oxalates. Unlike the others, it is not obtained as a dihydrate of the type $M^{II}C_2O_4{\cdot}2\ H_2O$ (M=Mn, Fe, Co, Ni, Zn).[10] However, early investigations by Schmittler[9a] already indicated that the small amount of water in CuC_2O_4 is not an integral part of the crystal lattice.[4, 7c] The dehydrated material was obtained after thermal treatment at 508 K in H_2 atmosphere.[9a] No single crystal-structure determination has been reported on moolooite or its synthetic analogue due to the lack of suitable

crystals.[9a, 9b, 11] Instead, structural information was deduced mainly from consistent powder XRD[9a, 9b] and EXAFS[12] investigations. In this respect, a combined neutron and

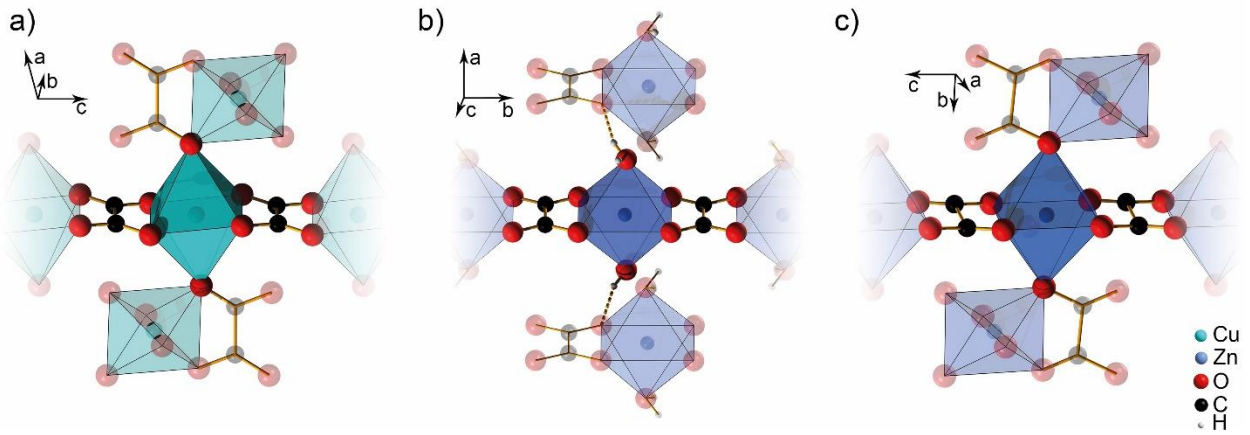

Figure 1: Metal coordination and ribbon-like motif present in the structure of CuC_2O_4 (a,), α-ZnC_2O_4 × 2 H_2O (b, ICSD card no: 56466) and β-ZnC_2O_4 (c, ICSD card no: 109665). Structure model of Christensen et al.[11] used for visualization of CuC_2O_4, stacking faults along *b* axis not shown.

X-ray powder diffraction study has been recently published.[11] Accordingly, Cu^{II} oxalate crystallizes in the monoclinic space group $P2_1/c$. The structure consists of a ribbonlike motif formed by planar -Cu-C_2O_4-Cu- bands along the *c* axis (Figure 1a).

Within in the ribbon, the divalent cation is coordinated by four oxygen atoms of two chelating, bridging oxalate ligands, and the two axial positions of the distorted octahedral environment are occupied by oxygen atoms of the adjacent ribbons in approximately perpendicular orientation. Thus, a three-dimensional structure is formed by interlinkage. In addition, stacking faults representing slips of the ribbons against each other are present along the *b* axis and lead to a disordered phase. The Cu^{II} ion with d^9 electron configuration shows the Jahn-Teller effect leading to distorted coordination geometries.[13] The dihydrate α-ZnC_2O_4·2 H_2O crystallizes in the monoclinic space group $C2/c$. Here, the divalent cation is coordinated by four oxygen atoms within the ribbonlike motif, and the octahedral coordination is completed by the oxygen atoms of two neighboring water molecules (Figure 1b).[10b] Thus, the ribbons are only interconnected indirectly by hydrogen bonds. Dehydration of this compound gives rise to the disordered α-ZnC_2O_4 (*Pnnm*) and the ordered β-ZnC_2O_4, which crystallizes in monoclinic space group $P2_1/n$

(Figure 1c).[14] $CuC_2O_4 \cdot n\ H_2O$ shares close structural resemblance with the latter polymorph (Figure 1), although the β-ZnC_2O_4 structure does not include stacking faults.[11,^14]

Successful isomorphous substitution by Zn^{II} in Cu^{II} oxalate has been rarely reported in the literature. In the thermal decomposition of a coprecipitated Cu/Zn oxalate (46.2^% Cu), Dalvi and Chavan[15] observed an anomalous single decomposition step, which they attributed to the formation of a metastable solid solution. On applying the oxalate gel/coprecipitation method to the ternary Cu/ZnO/Al_2O_3 system, Deng et al.[6a] reported the formation of the binary mixed-metal oxalate phase from ethanolic solution. The Zn^{II} oxalate phase is present at low Cu content (Cu/Zn<1/8) and vice versa (Cu/Zn>2). So far, a comprehensive study on the substitution of Cu and Zn oxalates in aqueous solutions has not been reported in the literature.

Herein, we present a study on successful Zn incorporation in Cu^{II} oxalate, ranging from the pure single-metal oxalates to equimolar ratios, and also address the existing structural limitations. At a constant pH value, coprecipitation from aqueous solution was used for the preparation of a complete set of mixed Cu/Zn oxalates. The obtained precipitates were thoroughly characterized by XRD, X-ray fluorescence (XRF), simultaneous thermal analysis/evolved-gas analysis (STA/EGA), and IR and Raman spectroscopy. Our findings provide valuable information on the boundaries of the limited solid-solution series of Cu/Zn oxalates and identify the regimes of perfectly dispersed Cu and Zn moieties.

Results and Discussion

Synthesis, composition, and structural analysis

Table 1: Overview of prepared oxalate samples including metal composition (XRF) and specific surface area determined by N_2 physisorption (SA_{BET}).

Sample	Exp. [at.-%]		SA_{BET} [m^2g^{-1}]
	Cu	Zn	
Zn_0	100	0	10
Zn_5	99.0	1.0	10
Zn_15	93.4	6.6	9
Zn_20	87.3	12.7	10
Zn_30	74.0	26.0	10
Zn_40	68.7	31.3	10
Zn_45	56.1	43.9	13
Zn_50	50.0	50.0	14
Zn_55	44.8	55.2	15
Zn_60	43.4	56.6	14
Zn_70	30.5	69.5	13
Zn_80	20.9	79.1	16
Zn_85	18.2	81.8	14
Zn_95	6.8	93.2	14
Zn_100	0	100	11

Coprecipitation was applied as a standard synthesis technique to study the formation of mixed Cu/Zn oxalates. Initial precipitation titration experiments (see Supporting Information, Figure S1) were conducted to find suitable reaction conditions for their coprecipitation using a $K_2C_2O_4$ solution as precipitating agent. On raising the pH value of the acidified mixed-metal solution (pH 0.1), Cu^{II} oxalate precipitates first, followed by the presence of α-$ZnC_2O_4 \cdot 2\ H_2O$ below pH 1.0. The formation of unwanted $K_2Cu(C_2O_4)_2 \cdot 2\ H_2O$ was observed above pH 1.8. Hence, coprecipitation from aqueous solution was performed at a fixed pH of 1.0 at 303 K (see Experimental Section). To investigate the limits of Zn^{II} incorporation into the Cu^{II} oxalate structure, the Zn content was incrementally increased from 0 to 100 % in a series of materials. All materials are named according to their nominal Zn contents (Table 1). The relative metal compositions derived by XRF (Table 1) are in agreement with the nominal values for all samples close

to and above the equimolar range. However, characteristic deviations are present in the compositional periphery. The samples up to a nominal value of 40 atom % Zn (Zn_40) show a pronounced lack of Zn in the precipitate. A similar observation has been reported in the case of Cu-rich mixed Cu/Zn basic formates $(Cu_{1-x}Zn_x)_2(OH)_3HCO_2$.[16] Despite thorough washing of the precipitate, minor potassium impurities were present in the materials. This has been previously observed when potassium oxalate was used as precipitating agent.[17]

The powder XRD patterns of the prepared series of materials are shown in Figure S2 (Supporting Information). The two materials obtained from the single-metal solutions show the diffraction pattern of crystalline Cu^{II} oxalate (JCPDS no. 21-297) in the case of Zn_0 and a diffraction pattern coinciding with JCPDS no. 25-1029 for Zn_100, that is, α-$ZnC_2O_4 \cdot 2\ H_2O$ rather than the structurally related β-ZnC_2O_4 was formed under the given reaction conditions. The patterns of materials containing up to nominal amounts of 95 atom % Zn share close resemblance to that of Cu^{II} oxalate. In this series, the incremental shift of particular reflections and changes in their peak shape can be observed owing to the increased Zn content x_{Zn}, which indicates incorporation of Zn^{II} in the Cu^{II} oxalate structure (Figure 2). This is further evidenced by the shift of the strong 110 reflection from 2θ=22.81 (Zn_0) to 23.44° (Zn_95). The peak shift is small in the Cu-rich region and pronounced for the Zn-rich materials. In the intermediate regime, the main peak exhibits a more complex structure with shoulder or double maximum, indicative of the presence of two overlapping peaks with variable ratios.

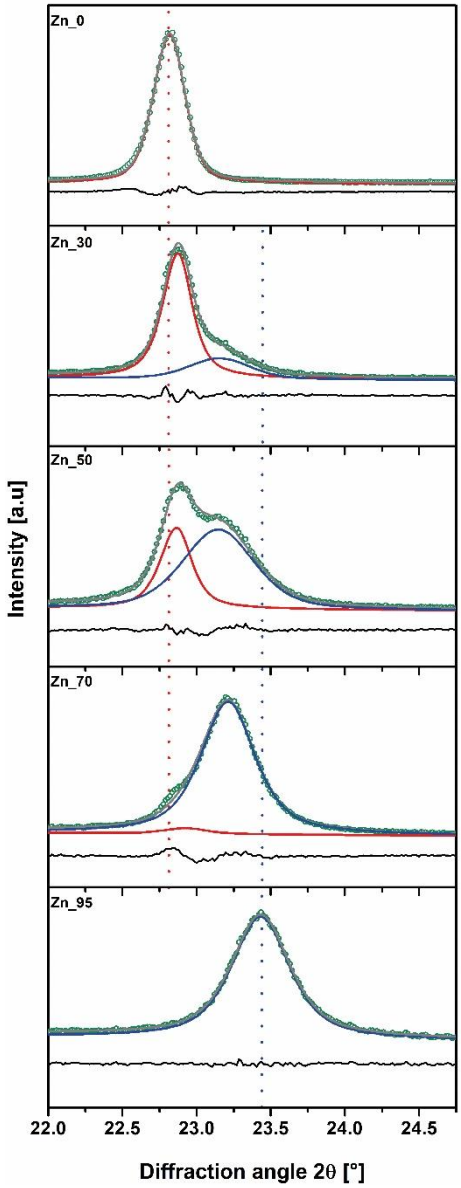

Figure 2: Shift of the 110 reflection as a function of χ_{Zn} in the Rietveld fits of selected Cu/Zn mixed oxalate samples. Experimental pattern (green circles), calculated curve (grey line) and difference curve (bottom line) are given, while the contribution of the Cu and Zn rich phases are shown in red and blue, respectively.

We tentatively interpreted this effect as being caused by two similar, coexisting phases resulting from a miscibility gap. The diffraction pattern of the pure Cu material was simulated in a Rietveld fit by using the disordered structure model of Christensen et al.[11] Their stacking-fault model consists of two alternative sets of atomic coordinates, which are identical except for a shift of the *z* coordinates by 0.5. Due to the stacking disorder,

the peak widths exhibit a pronounced anisotropy (*hkl* dependence), which could be described satisfactorily by a combination of isotropic size broadening and anisotropic strain broadening according to the Stephens model.[18] For the fit, the atomic coordinates published by Christensen et al. were kept constant,[11] but the occupancy ratio between the two disordered sets of coordinates was refined. The isotropic displacement parameters were arbitrarily set to B=1 Å^2, and the lattice parameters were refined. The same structure model and refinement procedure were then successfully applied to all other apparently single-phase diffraction patterns (except that of Zn_100), and this supported our initial hypothesis that the moolooite structure type persists up to very high Zn contents. The β-ZnC_2O_4 structure model of Kondrashev et al.[14] was also tested in comparison, but performed less well, even when the stacking disorder was added to the model. In the two-phase regime, however, the extensive peak overlap within and between the two phases in conjunction with the anisotropic peak broadening did not allow the extraction of reproducible lattice parameters by using two freely refined phases of the moolooite type because of too many refinable parameters. Thus, the fit model was restricted on the basis of chemical reasoning. The two-phase regime in a miscibility gap is typically characterized by the coexistence of two phases that have constant properties (e.g., stoichiometry, lattice parameters) but vary continuously in their mixing ratio. Hence, all eight diffraction patterns of this range were fitted simultaneously in a single refinement. The lattice parameters were coupled across the whole biphasic regime, that is, they were restrained to have identical values for all data sets, for both the copper-rich and the zinc-rich phase. In contrast, the peak shape parameters, disorder parameters, and scale factors (phase amounts) were still refined individually. As a result, all included patterns were fitted sufficiently well to corroborate our model and yielded not only stable lattice parameters but also approximate amounts of phases (Figure 3).

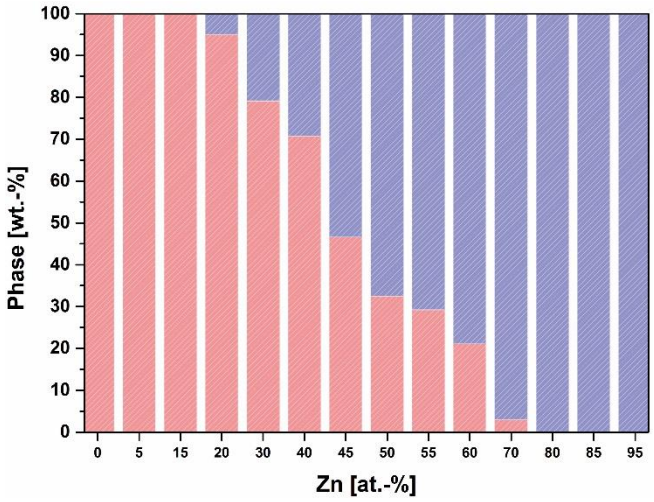

Figure 3: Diagram of state showing the proportion of Cu-rich (red) and Zn-rich (blue) mixed Cu/Zn oxalate phases as a function of the nominal Zn content as derived from the corresponding Rietveld analysis.

Note that the electron densities of Cu and Zn are too similar to be distinguished by XRD under such conditions. Furthermore, only the integral composition of the samples, but not of the individual phases in the two-phase region, is known from elemental analysis. Thus, all fits were performed with only Cu atom on the metal sites of the structure model, which led to small systematic deviations in the XRD-based determination of the phase amounts. All in all, single-phase synthetic mixed-metal oxalates are obtained up to a Zn content of 6.6 atom % (Zn_15). When the Zn content exceeds this value a second phase is found, and with a further increase of the Zn content up to 69.5 atom % (Zn_70), its fraction increases (Figures 2 and 3) and again the monophasic state is reached at compositions with ≥79.1 atom % Zn (Zn_80). The graphical representation of all Rietveld fits is given in Figures S3 and S4 of the Supporting Information for the Cu-rich and Zn-rich materials, respectively. The corresponding lattice parameters are summarized and compared to selected literature values in Table S2 of the Supporting Information.

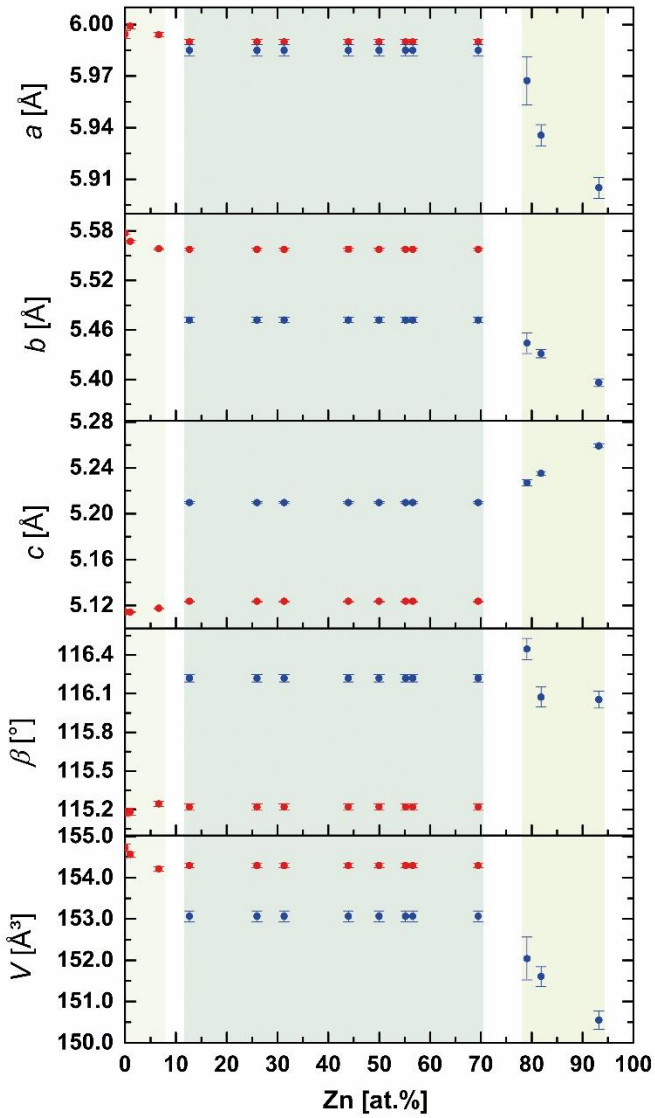

Figure 4: Trends of lattice parameters *a*, *b* and *c*, the monoclinic angle *β* and the unit-cell volume V in the oxalate sample series as a function of Zn content determined by XRF. Error bars of 3ESD (estimated standard deviations) are given. Single phase (light green) and binary phase (dark green) regions highlighted. The constancy of lattice parameters in the two-phase regime is a result of the restrictive coupled fit model.

The evolution of the lattice parameters *a*, *b*, and *c*, the monoclinic angle *β*, and the unit-cell volume V as a function of the Zn content is shown in Figure 4 (data in Table S2 of the Supporting Information). Both the Cu-rich and Zn-rich phases show the same qualitative trends in their respective single-phase regimes, which are also represented in the comparison of the two phases with each other: with increasing Zn content, the lattice parameters *a* and *b* decrease while *c* and *β* increase. Overall, this results in a reduction of the unit-cell volume with increasing Zn substitution. SEM analysis of selected samples

was performed to investigate the morphological changes that were expected to be present in the proposed limited solid-solution series of Cu/Zn oxalates. The SEM images of Zn_5, Zn_50, and Zn_95 are shown in Figure 5. At a low degree of Zn^{II} incorporation into the CuC_2O_4 lattice (Figure 5a) the obtained rounded, spherelike particles of varying micrometer sizes feature a porous texture and close similarity to the pure Cu oxalate material (Figure S5 in the Supporting Information). The Zn_95 material (Figure 5c) differs drastically. It consists of stacked-prismatic to tabular-shaped aggregates with a rough texture clearly identical to that of the Zn_100 material (Figure S6 in the Supporting Information). The material with Cu/Zn parity (Figure 5b) consists of both aforementioned morphological motifs. This is in agreement with the presence of two mixed-metal oxalate phases in the proposed miscibility gap. With increasing Zn content, the BET specific surface area slightly increases from about 10 to 14 m^2g^{-1}.

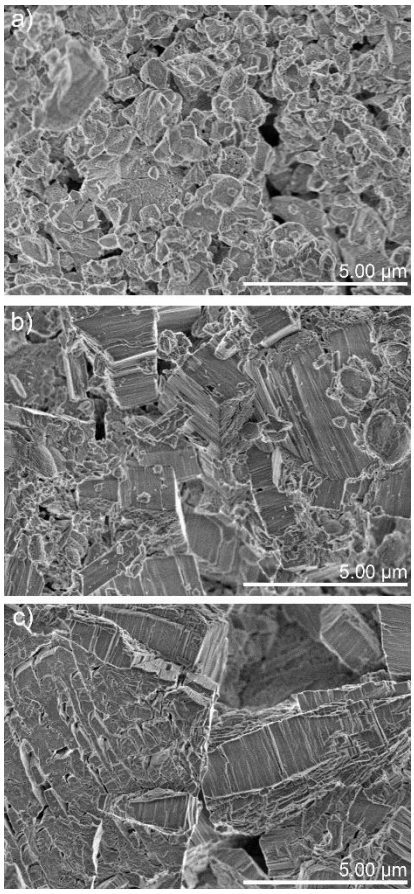

Figure 5: SEM micrographs of the Cu: Zn-samples Zn_5 (a), Zn_50 (b) and Zn_95 (c).

Thermal analysis

The thermal behavior of all materials was investigated by STA/EGA in 21 % O_2/Ar up to 770 K. The STA results for the Cu-rich and Zn-rich materials are shown in Figures S9 and S10 of the Supporting Information, respectively. For all materials the presence of the corresponding metal(II) oxides was verified by XRD analysis after thermal treatment (Figure 6b and Figure S12 in the Supporting Information).

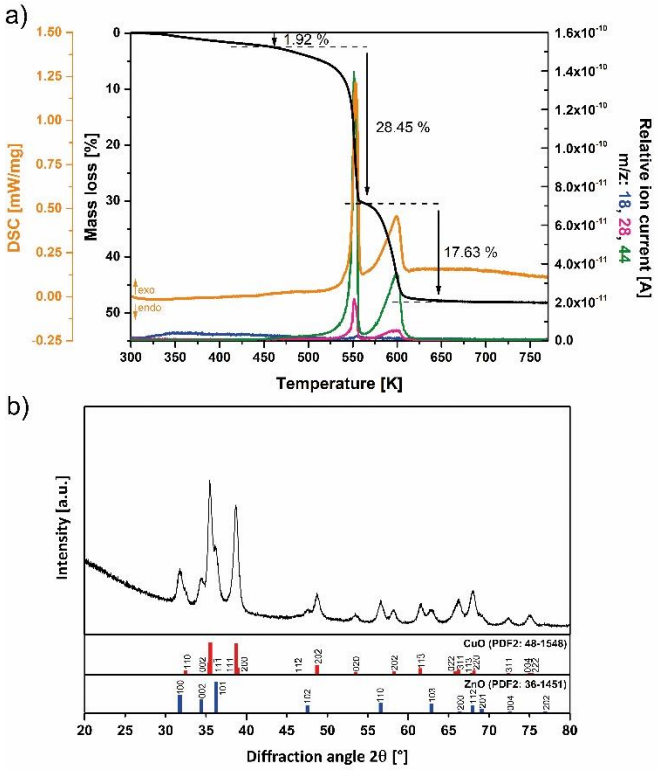

Figure 6: Exemplary STA and EGA results of Zn_40 sample (a) and XRD analysis after thermal analysis (b). Mass loss (black line), DSC curve (orange line) and mass spectrometer signals of H_2O (m/z 18, blue line), CO (m/z 28, magenta line) and CO_2 (m/z 44, green line) are given.

According to Dollimore et^^al., the decomposition of the pure oxalates of Cu^{II} and Zn^{II} in inert atmosphere takes place according to reactions (1) and (2)[19]:

$CuC_2O_4 \rightarrow Cu + 2\ CO_2$ (1)

$ZnC_2O_4 \rightarrow ZnO + CO + CO_2$ (2)

The product of the thermal breakdown of Cu^{II} oxalate strongly depends on the chosen atmosphere.[20] In 21 % O_2/Ar the thermal decomposition of the oxalate anion of pure Cu^{II} oxalate (Zn_0) takes place as an exothermal event located at a peak temperature of 534 K (Figure S9a in the Supporting Information). $Cu^{II}O$ was obtained as the final solid product (Figure S12 in the Supporting Information). The formation of Cu^{I}_2O was not observed, but its presence as an intermediate towards $Cu^{II}O$ cannot be ruled out. Thus, the generalized Equation (3) is given. The interpretation of the reaction scheme in air has been debated in the literature.[7c,21] However, the detailed investigation of the reaction path of pure Cu^{II} oxalate is beyond the scope of this paper.

$CuC_2O_4 \rightarrow [Cu_2O, Cu] \rightarrow CuO$ (3)

In the case of Zn^{II} oxalate (Zn_100) the decomposition step is shifted to higher temperature and is present as an endothermal event at 635 K coinciding with the release of CO and CO_2 (Figure S10h in the Supporting Information). Independent of the applied atmosphere, it follows endothermal decomposition reaction (2).[7a,20,22] Whereas the thermal decomposition of Cu^{II} oxalate is always exothermic,[20] this only holds for Zn^{II} oxalate in oxygen-containing atmosphere when the secondary exothermic oxidation of CO to CO_2 takes place.[22b] Besides, the distinct endothermal loss of crystallization water of the dihydrate is observed at 340 - 470^^K. The discussed results for both single metal oxalates agree very well with the literature.[7a,7c,19a,20,22a,b,23] Thus, the decomposition temperature of the oxalate anion is taken as a valuable approximation of Zn^{II} incorporation into the CuC_2O_4 lattice for materials exhibiting a single decomposition step between 534 and 635 K (in contrast to two separate ones; Figure7).

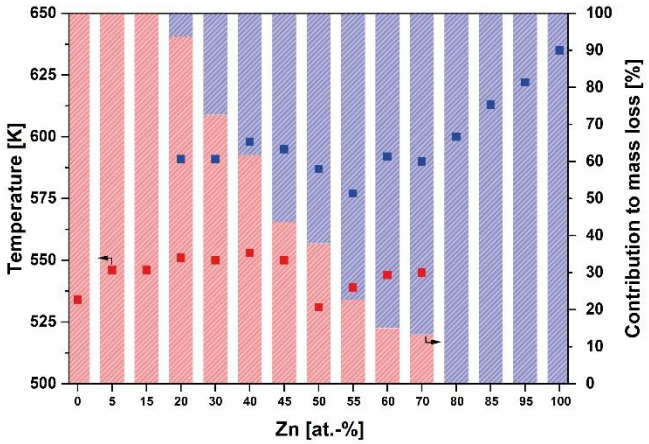

Figure 7: Effect of Zn content on the decomposition temperature of Cu-rich (red) and Zn-rich (blue) mixed Cu/Zn oxalate phases and their relative contribution to the observed mass loss. Nominal Zn content given. Peak temperatures of DSC events and detected mass loss during oxalate anion decomposition according to Table S3.

The observation of single oxalate decomposition events at the peripheries of the mixed Cu/Zn oxalate systems is in excellent agreement with the presented XRD analysis and further evidences the formation of a limited solid-solution series. As expected, with increasing Zn content the characteristic exothermic peak is shifted to higher onset temperatures (Figure S11 in the Supporting Information), and the decomposition is completed at a distinctly lower temperature than for pure Zn^{II} oxalate. This clearly differs in the case of a physical mixture of both oxalates, for which no pronounced effect on the thermal behavior of the two components has been reported.[24] The complexity of this system is further indicated by the anomalous decrease in the decomposition temperatures of the two separate mixed-metal oxalate phases in the biphasic regime in the cases of Zn_50 and Zn_55. Furthermore, Cu-rich materials exhibit sharper signals in the differential scanning calorimetry (DSC) curve and a minor initial slow mass loss due to dehydration (<5 %), whereas some Zn-rich materials (e.g., Zn_80) show a distinct dehydration event around 375 K and overall broader decomposition signals. The theoretical and experimental weight losses on thermal decomposition are summarized in Table S3 in the Supporting Information and are in excellent agreement.

Vibrational spectroscopic analysis

ATR-IR and Raman spectra were recorded to investigate changes of the local -C_2O_4-M-C_2O_4- environment induced by incremental Zn incorporation into the CuC_2O_4 structure (Figures8 and 9, respectively). For both CuC_2O_4 (Zn_0) and α-ZnC_2O_4·2 H_2O (Zn_100) the obtained IR and Raman spectral patterns (Figure S13 and Figure S14) are in excellent agreement with the literature.[9c,10c,25] Since all materials up to a nominal value of 95 atom % Zn show close resemblance to Cu^{II} oxalate (see XRD analysis), it serves as the basis for the assignment [9c,25] of the observed vibrational modes (Tables S4 and S5 in the Supporting Information). To the best of our knowledge, vibrational spectroscopic data of β-ZnC_2O_4,[14] structurally closely related to CuC_2O_4, have not been reported in the literature so far.

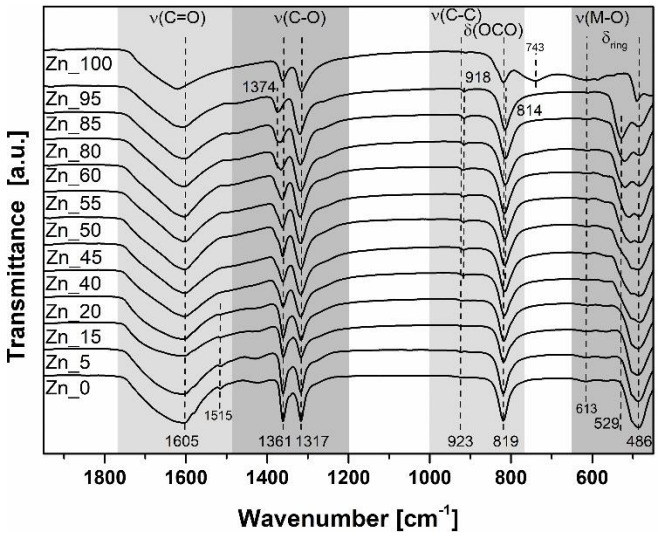

Figure 8: Evolution of ATR-IR spectra as a function of nominal Zn content. The extended spectrum up to 3850 cm^{-1} is presented in Figure S15.

The evolution of the ATR-IR spectra with increasing Zn content is shown in Figure 8. The spectra increasingly deviate from that of the single-metal oxalate CuC_2O_4 (Zn_0) with increasing Zn content. The ATR-IR spectrum of the CO stretching region shows a broad

asymmetric band around 1605 cm^{-1} assigned to $\nu_{as}(CO)$ with a fluctuation of ±3 cm^{-1} in the series up to a nominal Zn content of 95 atom %. Additionally, two intense vibrational bands from $\nu_s(CO)$ and δ(OCO) modes centered at about 1300 cm^{-1} (1361 and 1317 cm^{-1} for Zn_0) are broadened with increasing Zn content (not affected by ATR correction, Figure S15 in the Supporting Information). The former shifts to higher wavenumbers of 1374 cm^{-1}, whereas the latter merely alters its position to 1319 cm^{-1} (+2 cm^{-1}) The weak ν(CC) band at 923 cm^{-1} and strong δ(OCO) band at 819 cm^{-1} both move to slightly lower energies (-5 cm^{-1}). Besides, Zn_100 and Zn_80 show, in agreement with their thermal analysis, a broad feature assigned to the $\rho(H_2O)$ mode at 743 cm^{-1} and the ν(OH) mode at 3360 cm^{-1} (Figure S15 in the Supporting Information). It is assumed that the $\delta(H_2O)$ band overlapped with the distinct $\nu_{as}(CO)$ band. The observed signals in the range from 650 to 450 cm^{-1} are assigned to metal-oxygen stretching vibrations and deformation modes of both the oxalate ions and the metal-oxygen moieties.[25a,25b] With higher Zn content, the signals get sharper and the intensity varies. Two distinct bands are visible, one at 486 cm^{-1}, which loses intensity with increasing Zn content, and another at 529 cm^{-1}, which moves slightly to lower wavenumbers with decreasing Zn content. The second band is visible as a shoulder of the main signal at 486 cm^{-1} at the parity ratio of Cu and Zn. Generally, all spectroscopic features are related to CuC_2O_4 and β-ZnC_2O_4 (for the materials Zn_0 to Zn_95) or α-$ZnC_2O_4 \cdot 2\ H_2O$ (for Zn_100), which is completely in line with the results from powder XRD and thermal analysis. Complementary to the IR analysis, Raman measurements were conducted. The vibrational motifs of all materials were qualitatively comparable to the IR data. The spectra are shown in Figure 9. The Raman spectra of the CO stretching region feature two low-intensity bands, at 1666 and 1616 cm^{-1}, both of which are hardly a function of Zn content. Besides, the strong $\nu_{as}(CO)$ band at 1518 cm^{-1} and the band at 1489 cm^{-1} [$\nu_s(CO)$+ν(CC)] are strongly affected by incremental increases in Zn content, which lead to pronounced changes in relative intensity. The asymmetric envelope is finally located at 1496 cm^{-1}. The weak ν(CC)/δ(OCO) bands at

924 and 833 cm^{-1} are shifted to slightly lower energy (-5 cm^{-1}) in the material series. In the deformation-mode region on the lower energy side of the spectrum, three bands are observed, initially located at 613, 588, and 561 cm^{-1}. With higher Zn content, the signals become broadened and their relative intensities change. Besides, a minor redshift is noted, especially for the signal at 561 cm^{-1}, which shifts to 545 cm^{-1}.

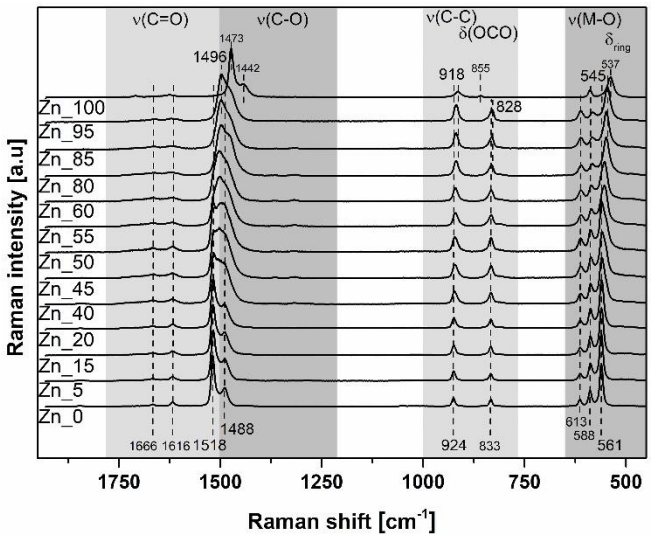

Figure 9: Evolution of Raman spectra as a function of nominal Zn content.

It is generally well established that all fundamental modes of the oxalate ion are affected by coordination with a metal (M) ion.[26] Furthermore, with decreasing M-C-O bond strength, the corresponding C-C-O bond becomes stronger, the free C-C-O bond gets weaker, and hence the energy gap of the ν_s and ν_{as} vibrational bands decreases.[26a] The degree of covalency of the M-C-O bond depends on the electronegativity (EN) of M. Zn (EN: 1.6) is less electronegative than Cu (EN: 1.9).[27] Thus, on incremental addition of Zn^{II} to the Cu^{II} oxalate lattice, a less covalent M-C-O interaction will probably occur in the mixed oxalate compared with pure single-metal CuC_2O_4.[24] In this light, the observed trend of energetic alignment of the ν_{as}(CO) and ν_s(CO) vibrational bands (Figure 9) indicates successful substitution. The observed band shifts are more pronounced at the compositional periphery (especially on the Zn-rich side). This could be due to the dampening effect of the envelope spectrum based on multiple phases contributing to the

overall measured spectrum around the parity ratio of Cu and Zn. The presence of a miscibility gap was already indicated by both XRD and thermal analysis.

Conclusion

We have reported on the successful synthesis of a series of mixed Cu/Zn oxalates by coprecipitation from aqueous solution at constant pH. Rietveld analysis of the powder XRD data indicated successful isomorphous substitution of Zn^{II} into the Cu^{II} oxalate lattice at the compositional peripheries (≤6.6 and ≥79.1 atom % Zn). Although Cu^{II} and Zn^{II} have similar ionic radii, which are well within the limits set by Goldschmidt,[28] they differ in their electron configuration. In this respect, Cu^{II} (d^9) is known to be affected by the Jahn--Teller effect, which leads to distorted coordination geometries. In contrast, Zn^{II} (d^{10}) prefers a symmetrical coordination environment. Thus, the formation of a continuous solid-solution series seems unlikely. The formation of a Cu-containing phase isostructural to α-ZnC_2O_4·2 H_2O, as reported by Deng et al.[6a] for coprecipitated materials from ethanolic solutions, was not verified. SEM analysis showed drastic morphological and textural changes. The miscibility gap is distinguished by the increasing amount of the Zn-rich solid solution with increasing Zn content. The addition of this second metal is reflected by a change of all lattice parameters leading to a contraction of the unit cell for the Zn-rich solid solution. Thermal analysis showed single decomposition events within the stated compositional boundaries, which shifted to higher temperature with increasing Zn content, whereas multiple events were observed near the 1:1 ratio of Cu and Zn. In addition, consistent relative phase contributions of both solid solutions in the miscibility gap were obtained by XRD and thermal analysis. Moreover, vibrational spectroscopy identified changes of the local environment induced by incremental Zn incorporation into the CuC_2O_4 structure. This established the compositional boundaries of the limited solid-solution series of mixed Cu/Zn oxalates. The presented work serves as an essential contribution to the successful

synthesis of single phase Cu/Zn oxalate precursors, potentially applicable in heterogeneous catalysis.

Experimental Section

General

All reagents were purchased from commercial vendors and used without further purification. For all experiments, ultrapure water, taken from a Milli-Q water treatment system (Merck Millipore), was used.

Synthesis

A 1.0 M aqueous solution containing the desired proportions of $Cu(NO_3)_2 \cdot 3\ H_2O$ (>99 %, Carl Roth) and $Zn(NO_3)_2 \cdot 6\ H_2O$ (>99 %, Sigma-Aldrich) was prepared. The pH was adjusted to 0.5 by addition of HNO_3 (>65 wt %, Carl Roth). The precipitating agent was aqueous 1.2 M $K_2C_2O_4 \cdot H_2O$ (>98 %, Carl Roth). The reaction vessel was filled with Millipore water (50 mL). With strict control of pH (pH 1.0) and temperature (303 K), the metal salt solution was added dropwise over 20 min with vigorous stirring. To keep the pH constant at 1.0, appropriate amounts of $K_2C_2O_4$ solution was added during the coprecipitation step. The precipitation was followed by an aging time of 5 min (303 K, pH 1.0). Afterwards, precipitate was collected by filtration or centrifugation (Rotina 380, Hettich) and washed several times with Millipore water until the conductivity of the washing medium was <0.5 mS cm^{-1}. The solid was dried at 353 K in air overnight and stored in a desiccator over silica gel orange.

Characterization

Powder XRD data were recorded with a STOE STADI P transmission diffractometer equipped with a primary focusing Ge monochromator for $Cu_{K\alpha1}$ radiation and a DECTRIS MYTHEN 1K position-sensitive solid-state detector. The finely ground sample powders were fixed between two layers of thin polyacetate film with small amounts of X-ray- amorphous grease before mounting. The

diffraction patterns were analyzed by full pattern fitting according the Rietveld method as implemented in the TOPAS software package (TOPAS version 5.0, 1999-2014, Bruker AXS).

Wavelength-dispersive XRF measurements were performed with a S4 PIONEER (Bruker AXS) spectrometer on 40 mm solidified-molten-glass sample disks. Quantification of the data was based on a ten-point reference curve.

SEM images were taken with a S-4800 (Hitachi) microscope equipped with a field-emission gun system. The sample was dispersed on a tape of conductive carbon (Plano). The instrument was operated at low accelerating voltage (1.5 kV) for increased resolution of the surface features of the sample.

The BET surface area [29] was obtained by N_2 physisorption at liquid-nitrogen temperature (77 K) by using an Autosorb-6B2-KR (Quantachrome). Prior to measurement, the samples were degassed at 353 K for 4 - 17.5 h with an Autosorb Degasser setup (Quantachrome).

STA measurements (TG/DSC) were conducted with an STA 449 C Jupiter thermoanalyzer (Netzsch) under a controlled gas atmosphere (21 % O_2/Ar, 100 mL min^{-1}), which was connected to a quadrupole mass spectrometer (QMS200 Omnistar, Balzers) for EGA by a quartz capillary heated to 313 K. Each measurement was performed with approximately 10 - 20 mg of sample in the temperature range of 300 – 773 K (2K min^{-1}). On cooling to room temperature, the residual powder sample was further analyzed by powder XRD. All data were analyzed with the NETZSCH Proteus Thermal Analysis software package (Version 6.10). Partial smoothing was applied to the STA and EGA data.

IR spectra of powder samples were recorded in a range of 45 - 6000 cm^{-1} (resolution: 1.0 cm^{-1}) at room temperature by using a Varian 670 FTIR spectrometer equipped with a diamond ATR unit (GladiATR, Pike). For this purpose, a 632.8 nm laser with a power of no more than 0.6 mW was used. Spectra were recorded with 256 scans for each sample after performing a background measurement (air).

Raman measurements were conducted with a TriVista raman microscope system (TriVista TR 557, S&I GmbH) equipped with a CCD detector (Spec10: 100BR, Pinceton Instruments) and a 10× objective lens. The sample was excited by a 532 nm laser (Samba CW DPSSL, Cobolt) with a laser power of 0.206 mW at most (600 gr mm^{-1} grating, resolution: 1 cm^{-1}). Calibration of the spectrometer frequency was performed by using a Si wafer (520.7±0.5 cm^{-1}). For each sample a mean-value spectrum based on a five-spot measurement is given.

Acknowledgements

The authors thank J. Allan for XRD and STA/EG measurements, M. Hashagen for BET measurements, A. K. Hoffman and Dr. O. Timpe for XRF analysis, W. Frandsen for SEM analysis and Dr. J. Noack for technical support in Raman measurements.

Conflict of interest

The authors declare no conflict of interest.

References

[1] a) A. Chebbi, P. Carlier, *Atmos. Environ.* **1996**, *30*, 4233 - 4249; b) M. L. Buch, *A Bibliography of Organic Acids in Higher Plants* Agricultural Research Service, U.S. Deptartment of Agriculture, Washington, D.C., **1960**.

[2] K.V. Krishnamurty, G. M. Harris, *Chem. Rev.* **1961**, *61*, 213 - 246.

[3] T. Echigo, M. Kimata, *Can. Mineral.* **2010**, *48*, 1329 – 1357.

[4] R. M. Clarke, I. R. Williams, *Mineral. Mag.* **1986**, *50*, 295 - 298.

[5] a) T. Ahmad, A. Ganguly, J. Ahmed, A. K. Ganguli, O. A. A. Alhartomy, *Arab. J. Chem.* **2011**, *4*, 125 - 134; b) F. Behnoudnia, H. Dehghani, *Polyhedron* **2013**, *56*, 102 - 108; c) A. Aimable, A. Torres Puentes, P. Bowen, *Powder Technol.* **2011**, *208*, 467 - 471; d) Z. Jia, L. Yue, Y. Zheng, Z. Xu, *Mater. Res. Bull.* **2008**, *43*, 2434 - 2440; e) K. G. Kanade, B. B. Kale, R. C. Aiyer, B. K. Das, *Mater. Res. Bull.* **2006**, *41*, 590

– 600; f) A. Tokeer, V. Sonalika, S. Niladri, G. Subhasis, K. G. Ashok, *Nanotechnology* **2006**, *17.*

[6] a) J. Deng, Q. Sun, Y. Zhang, S. Chen, D. Wu, *Appl. Catal. A* **1996**, *139*, 75 -85; b) Y. Zhang, Q. Sun, J. Deng, D. Wu, S. Chen, *Appl. Catal. A* **1997**, *158*, 105 - 120; c) Y. Ma, Q. Sun, D. Wu, W.-H. Fan, Y.-L. Zhang, J.-F. Deng, *Appl. Catal. A* **1998**, *171*, 45 - 55; d) Y. Ma, Q. Sun, D. Wu, W.-H. Fan, J.-F. Deng, *Appl. Catal. A* **1999**, *177*, 177 - 184; e) J. Agrell, K. Hasselbo, K. Jansson, S. G. Järås, M. Boutonnet, *Appl. Catal. A* **2001**, *211*, 239 - 250; f) Z.-s. Hong, Y. Cao, J.-f. Deng, K.-n. Fan, *Catal. Lett.* **2002**, *82*, 37 - 44; g) D. Lesmana, H.-S. Wu, *Energy* **2014**, *69*, 769 - 777.

[7] a) D. Dollimore, *J. Therm. Anal. Calorim.* **1977**, *11*, 185 - 200; b) E. A. Gusev, S. V. Dalidovich, V. A. Shandakov, A. A. Vecher, *Thermochim. Acta* **1985**, *89*, 391 - 394; c) B. Donkova, D. Mehandjiev, *J. Mater. Sci.* **2005**, *40*, 3881 - 3886.

[8] F. Schüth, M. Hesse, K. K. Unger, in *Handbook of Heterogeneous Catalysis*, Wiley-VCH, Weinheim, **2008**.

[9] a) H. Schmittler, *Monatsber. Dtsch. Akad. Wiss. Berlin* **1969**, *10*, 581 - 604; b) H. Fichtner-Schmittler, *Cryst. Res. Technol.* **1984**, *19*, 1225 - 1230; c) R. L. Frost, J. Yang, Z. Ding, *Chin. Sci. Bull.* **2003**, *48*, 1844 - 1852.

[10] a) R. Deyrieux, A. Péneloux, *Bull. Soc. Chim. Fr.* **1969**, 2675 - 2681; b) R. Deyrieux, C. Berro, P. A, *Bull. Soc. Chim. Fr.* **1973**, 25 - 34; c) A. Wladimirsky, D. Palacios, M. C. D'Antonio, A. C. González-Baró, E. J. Baran, *J. Argent. Chem. Soc.* **2011**, *98*, 71-77; d) E. J. Baran, *J. Coord. Chem.* **2014**, *67*, 3734 - 3768.

[11] A. N. Christensen, B. Lebech, N. H. Andersen, J.-C. Grivel, *Dalton Trans.* **2014**, *43*, 16754 - 16768.

[12] a) A. Michalowicz, J. J. Girerd, J. Goulon, *Inorg. Chem.* **1979**, *18*, 3004 - 3010; b) A. Michalowicz, R. Fourme, *Acta Crystallogr. Sect. A* **1981**, *37*, C307.

[13] B. Murphy, B. Hathaway, *Coord. Chem. Rev.* **2003**, *243*, 237 - 262.

[14] Y. D. Kondrashev, V. S. Bogdanov, S. N. Golubev, G. F. Pron, *J. Struct. Chem.* **1985**, *26*, 74 – 77.

[15] B. D. Dalvi, A. M. Chavan, *J. Therm. Anal. Calorim.* **1978**, *14*, 331 – 334.

[16] M. Behrens, S. Kißner, F. Girsgdies, I. Kasatkin, F. Hermerschmidt, K. Mette, H. Ruland, M. Muhler, R. Schlögl, *Chem. Commun.* **2011**, *47*, 1701 – 1703.

[17] A. D. Keeble, Durham University (Durham University), **1990.**

[18] P. Stephens, *J. Appl. Crystallogr.* **1999**, *32*, 281 – 289.

[19] a) D. Dollimore, *Thermochim. Acta* **1987**, *117*, 331 – 363; b) D. Dollimore, D. L. Griffiths, D. Nicholson, *J. Chem. Soc.* **1963**, 2617 – 2623.

[20] D. Dollimore, D. Griffiths, *J. Therm. Anal. Calorim.* **1970**, *2*, 229 – 250.

[21] E. Lamprecht, G. M. Watkins, M. E. Brown, *Thermochim. Acta* **2006**, *446*, 91 -100.

[22] a) D. Dollimore, D. Nicholson, *J. Chem. Soc.* **1964**, 908 - 915; b) R. Majumdar, P. Sarkar, U. Ray, M. Roy Mukhopadhyay, *Thermochim. Acta* **1999**, *335*, 43 - 53; c) M. A. Mohamed, A. K. Galwey, S. A. Halawy, *Thermochim. Acta* **2005**, *429*, 57 -72.

[23] D. Dollimore, T. A. Evans, Y. F. Lee, *Thermochim. Acta* **1992**, *194*, 215 - 220.

[24] M. A. Gabal, *Thermochim. Acta* **2003**, *402*, 199 – 208.

[25] a) H. G. M. Edwards, D. W. Farwell, S. J. Rose, D. N. Smith, *J. Mol. Struct.* **1991**, *249*, 233 – 243; b) M. C. D'Antonio, D. Palacios, L. Coggiola, E. J. Baran, *Spectrochim. Acta Part A* **2007**, *68*, 424 - 426; c) K. Muraleedharan, S. Kripa, *J. Therm. Anal. Calorim.* **2014**, *115*, 1969 – 1978.

[26] a) K. Nakamoto, J. Fujita, S. Tanaka, M. Kobayashi, *J. Am. Chem. Soc.* **1957**, *79*, 4904 - 4908; b) M. J. Schmelz, T. Miyazawa, S.-I. Mizushma, T. J. Lane, J. V. Quagliano, *Spectrochim. Acta A* **1957**, *9*, 51 - 58.

[27] A. F. Holleman, E. Wiberg, N. Wiberg, *Lehrbuch der Anorganischen Chemie*, de Gruyter, Berlin/New York, **2007**.

[28] V. M. Goldschmidt, *Naturwissenschaften* **1926**, *14*, 477 – 485.

[29] S. Brunauer, P. H. Emmett, E. Teller, *J. Am. Chem. Soc.* **1938**, *60*, 309 – 319.